Journal of Alloys and Compounds 838 (2020) 155623

Contents lists available at ScienceDirect

Journal of Alloys and Compounds

journal homepage: http://www.elsevier.com/locate/jalcom

The mechanism of enhanced ionic conductivity in $Li_{1.3}Al_{0.3}Ti_{1.7}(PO_4)_3$–$(0.75Li_2O \cdot 0.25B_2O_3)$ composites

K. Kwatek [a, *], W. Ślubowska [a], C. Ruiz [b], I. Sobrados [b], J. Sanz [b], J.E. Garbarczyk [a], J.L. Nowiński [a]

[a] Warsaw University of Technology, Faculty of Physics, 00-662, Warsaw, Poland
[b] Instituto de Ciencia de Materiales de Madrid (ICMM CSIC), Madrid, Spain

ARTICLE INFO

Article history:
Received 27 March 2020
Received in revised form
11 May 2020
Accepted 12 May 2020
Available online 18 May 2020

Keywords:
Composite
Ceramic
NASICON
Glass
Solid electrolyte
All-solid state batteries

ABSTRACT

The oxide-based Li^+ conductors are considered as potential solid electrolytes for lithium-ion batteries. Among the NASICON–type materials, $Li_{1.3}Al_{0.3}Ti_{1.7}(PO_4)_3$ (LATP) seems to be a promising candidate for application. Although its bulk conductivity is of the order of 10^{-3} S · cm^{-1}, and seems to be sufficient for practical use, the total conductivity is considerably limited by the highly resistant grain boundaries. This shortcoming may be overcome by the formation of LATP–based ceramics with appropriate sintering aids. In this study, the $0.75Li_2O \cdot 0.25B_2O_3$ (LBO) glass with low melting point was chosen to improve the ionic conductivity of LATP. The properties of $Li_{1.3}Al_{0.3}Ti_{1.7}(PO_4)_3$–$y$ $(0.75Li_2O \cdot 0.25B_2O_3)$ $(0 \leq y \leq 0.3)$ system were studied by means of: high temperature X-ray diffractometry (HTXRD), $^6Li/^7Li$, ^{11}B, ^{27}Al and ^{31}P magic angle spinning nuclear magnetic resonance spectroscopy (MAS NMR), thermogravimetry (TG), scanning electron microscopy (SEM), impedance spectroscopy (IS) and density methods. Based on the experimental results, it is shown that the use of LBO glass as a sintering aid results in the enhancement of the total ionic conductivity of LATP ceramics. The correlations between apparent density, microstructure, composition, sintering temperature and ionic conductivity are presented and discussed. The presumed mechanism of the conductivity enhancement is analyzed in terms of the brick-layer model (BLM). The highest value of the total ionic conductivity, equal to 1.9×10^{-4} S · cm^{-1}, was obtained for LATP–0.1LBO sintered at 800 °C.

1. Introduction

Further development of the lithium-ion battery (LIB) technology may be achieved by the replacement of liquid electrolytes by solid counterparts. This solution offer many advantages related to improved safety, longer lifetime as well as higher energy and power density of the new generation of lithium-ion cells. It is noteworthy that all-solid-state lithium-ion batteries (ASSLIBs) should also exhibit better mechanical and thermal properties as well as wider electrochemical window, allowing for the use of new, high voltage (>5 V) cathode materials [1–4].

In order to be applicable as solid electrolyte, material is supposed to have a relatively high value of the total ionic conductivity, exceeding 10^{-4} S · cm^{-1} [1–5]. Unfortunately, most of the solid Li^+ conductors fulfilling this condition suffer from poor chemical stability against moisture, for example glasses based on Li_2S [1–4]. And conversely, the compounds sufficiently stable against moisture (mainly oxide-based compounds) exhibit low total ionic conductivity for practical use [1–5]. Therefore, the enhancement of electric properties of oxide-based materials seems to be an efficient way to elaborate a solid electrolyte with desirable properties required by the ASSLIB technology.

Lithium aluminum titanium phosphate of chemical formula $Li_{1+x}Al_xTi_{2-x}(PO_4)_3$ (LATP) is one of the promising candidates for application as solid electrolyte for ASSLIBs [6–17]. It crystallizes in NASICON structure with rhombohedral symmetry and belongs to R-3c space group. Its good thermal, mechanical and chemical stability as well as non-flammability are the essential features of the solid electrolyte material. Depending on the preparation procedure, the LATP grain interior exhibits high lithium ion conductivity in the range from 10^{-4} to 10^{-3} S · cm^{-1} at room temperature [6–18]. However, considering the application of a material as solid electrolyte not only the grain conductivity should be taken into

* Corresponding author.
E-mail address: konrad.kwatek@pw.edu.pl (K. Kwatek).

https://doi.org/10.1016/j.jallcom.2020.155623
0925-8388/

account, but overall conductivity [6–18]. Preparation of the ceramic material by a conventional solid-state reaction method, yields the total ionic conductivity from 10^{-6} to 10^{-4} S · cm^{-1} at room temperature [15–20]. Whereas, in the case of melt-quenching and sol-gel methods, the total conductivity may be as high as 10^{-3} S · cm^{-1} at room temperature [19–30]. Although, those synthesis methods lead to the formation of highly conducting material, they also suffer from some disadvantages. For instance, a sol-gel reaction method usually requires expensive reagents and therefore the use of that technology on an industrial scale is not cost-effective. As for the melt-quenching method, the limiting factor is the necessity of operating at high temperatures (above 1300 °C) necessary to melt the substrates.

Another approach explored in literature to obtain a highly conductive materials, consists on the addition of foreign phases into the base compound (called matrix) to lower both sintering temperature and grain boundary resistance [31–43]. This concept has been applied for many different kinds of ceramics. Since the preparation of ceramic material requires sintering at high temperatures, the addition of appropriate sintering agent in form of a glass with a low glass transition temperature and a low melting point after crystallization is supposed to be a good choice. During heat treatment, glass should transform into a liquid phase, which can efficiently both cover the grains and fill the pores, facilitating the densification process and lowering the sintering temperature.

Many literature reports show that the $0.75Li_2O \cdot 0.25B_2O_3$ glass is a very efficient sintering additive due to its low melting point. N.C. Rosero-Navarro et al. [42,43] reported high values of the total ionic conductivity in the $Li_7La_3Zr_xM_{1-x}O_{12} - Li_3BO_3$ (M = Nb, Ta) system when it is sintered at 900 °C. It was found that LBO glass prompts formation of the cubic LLZO phase and play an essential role in lowering the sintering temperature (from about 1100 °C to 900 °C), while maintaining good ionic properties. Also, E.A. Il'ina et al. [33,34] reported that stabilization of highly conducting cubic phase of $Li_7La_3Zr_2O_{12}$ could be done while $Li_2O–Y_2O_3–SiO_2$ or $Li_2O–B_2O_3–SiO_2$ glasses are added to the base material. Likewise, Aono et al. investigated the $LiTi_2(PO_4)_3–Li_3BO_3$ and $LiTi_2(PO_4)_3–Li_3PO_4$ systems and observed an enhancement of the total ionic conductivity comparing to the $LiTi_2(PO_4)_3$ base material [36]. Our previous works devoted to LTP–based composites with glassy $0.75Li_2O \cdot 0.25B_2O_3$ [37] or $1.35Li_2O \cdot 0.45B_2O_3 \cdot 0.1Li_2SO_4$ (LBSO) [38] additives, confirm the crucial role of the sintering agents in enhancement of total ionic conductivity. Also, N. Sharma et al. presented that composites based on LTP with addition of $60Li_2SO_4 \cdot 40LiPO_3$ [40] or $LiCl–P_2O_5$ [41] glasses exhibit better electrical properties in comparison to ceramic LTP. The authors claim that lithium ions present in the glassy phase may play an important role in the improvement of grain boundary conductivity. In yet another study, T. Hupfer et al. [32] showed that addition of $LiTiOPO_4$ to the LATP resulted in densification of material, yielding better electrical properties. These results also confirmed that the formation of a composite may be an efficient way to lower the sintering temperature for the LATP ceramics.

Here, we adopt this tactic to LATP–LBO system in order to obtain highly conductive material. Although this approach has been already employed in our previous study on LATP–LBSO system [35], here, besides using a new sintering agent, we extend the scope of our research by performing ^{6}Li MAS NMR experiment. Moreover, we put greater emphasis on changes in phase composition at different sintering temperatures. Therefore, this paper should provide useful information regarding the processing of LATP–based ceramics, especially as for the selection of their optimal sintering temperature. Moreover, MAS NMR results permit a better interpretation of a conductivity enhancement mechanism achieved in LATP–LBO composites. Based on the obtained results we propose and discuss a possible model of compositional and structural changes in LATP–LBO composites leading to the enhancement of their total ionic conductivity.

2. Experimental

Polycrystalline $Li_{1.3}Al_{0.3}Ti_{1.7}(PO_4)_3$ compound was obtained by means of a conventional solid-state reaction method. Reagent-grade chemicals, Li_2CO_3 (Sigma Aldrich), $NH_4H_2PO_4$ (POCh), anatase TiO_2 (Sigma Aldrich) and Al_2O_3 (Sigma Aldrich), were weighted in stoichiometric amounts, ground with mortar and pestle and synthesized in alumina crucible at 900 °C for 10 h.

$0.75Li_2O \cdot 0.25B_2O_3$ glass was obtained via a standard melt-quenching method. Stoichiometric amounts of reagents: Li_2CO_3 (Sigma Aldrich) and H_3BO_3 (POCh) were weighted, ground with mortar and pestle, placed in alumina crucible and annealed at 1100 °C for 15 min. Next, the annealed mixture of molten reagents was quenched rapidly between two stainless steel plates. Then, the obtained glassy plates were ball-milled with rotation speed of 400 rpm for 1 h in planetary mill Fritsch Pulverisette 7. Subsequently, the obtained LBO powder was added to as-prepared LATP material in molar ratio varying from 10 to 30%. Next, both components were ball-milled in ethanol at 400 rpm for 1 h, dried and pelletized under uniaxial 10 MPa pressure. Finally, pellets of 6 mm in diameter and ca. 2 mm thick, were formed and sintered at 700, 800 or 900 °C for 2 h.

Phase composition of the as-synthesized materials and composite powders after heat treatment were examined by means of X-ray diffraction method. Data were collected in the 2θ range from 10° to 90° with 0.05° step and counting rate of 0.5 s per step with CuKα line by means of a Philips X'Pert Pro diffractometer. Additionally, temperature dependent XRD (HTXRD) was performed in the temperature range from 30 to 900 °C using an Anton Paar HTK–1200 oven.

Thermal stability of the composites was determined by thermal gravimetric analysis (TGA). A TA Instruments Q600 calorimeter was used to register the mass loss and the temperature difference (with reference to empty alumina crucible) during heating under air flow in the temperature range from 50 to 900 °C. The measurements were performed at the heating rate of 10 °C.min^{-1} on powdered samples of ca. 20 mg each.

Apparent density of the pelletized samples was determined by Archimedes method with isobutanol as an immersion liquid. The accuracy of this method was estimated as ca. 1%. The microstructure of freshly fractured pellets was investigated by means of the scanning electron microscopy (SEM) employing a Raith eLINE plus setup.

For impedance spectroscopy measurements, both bases of the as-formed pellets were polished and covered with graphite as electrodes. Impedance investigations were carried out using a Solatron 1260 frequency analyzer in the frequency range from 10^{-1}–10^7 Hz in the temperature range from 30 to 100 °C, during both heating and cooling runs.

^{27}Al, ^{6}Li/^{7}Li, ^{31}P and ^{11}B MAS NMR spectra were acquired with a Bruker AVANCE-400 spectrometer (9.4T magnetic field). The used frequencies were equal to: 104.3, 58.8/155.4, 161.9 and 128.4 MHz, respectively. NMR spectra were recorded after 2.0 μs irradiation for aluminum, lithium and boron, 4.0 μs irradiation ($\pi/2$ pulses) for phosphorus with the MAS technique (rotation of samples at 10 kHz around an axis inclined 54°44′ with respect the external magnetic field). The number of scans was in the range from 100 to 800. Chemical shift values of NMR resonances were referred to 1 mol L^{-1} $AlCl_3$, 1 mol L^{-1} LiCl, 85 wt% H_3PO_4 and 0.3 mol L^{-1} H_3BO_3 aqueous solutions. The NMR spectra were simulated using *dmfit* software [44].

The PFG NMR technique was used to determine lithium diffusion coefficient in LATP and LATP–LBO samples. "Estimulated Echo" experiments were carried out with gradient pulse intensity varying from 100 to 2600 G m^{-1}. In these experiments $\pi/2$ pulses of 5 μs were used. The dependence of diffusion coefficients on the diffusion Δ time (interval between gradient pulses) was investigated. Also, the PFG NMR studies of the LATP–LBO ceramics were performed at elevated temperatures.

3. Results and discussion

3.1. X–ray diffraction

Fig. 1 presents X-ray diffraction patterns for polycrystalline (also referred as *pristine* or *as-prepared*) LATP before sintering and LATP–0.2LBO composite before and after sintering at 900 °C for 2 h. As for the pristine LATP material, the positions and relative intensities of the main reflections correspond to the NASICON structure with R-3c symmetry group (ICDD 00-035-0754). One can also observe some weak diffraction lines at 2θ angles 20.6° and 26.3° which were identified and ascribed to TiO_2 anatase and $AlPO_4$ berlinite phases, respectively [10,15,16,20,23,24,27,31,45,46]. The comparison of X-ray diffraction patterns of polycrystalline LATP and non–sintered composite, do not display any important differences. However, more significant differences are noticeable on diffraction pattern for LATP–0.2LBO sintered at 900 °C which exhibits new reflections at: 27.0, 27.4, 28.0 and 39.6° belonging to $LiTiPO_5$ (ICDD 00–044–0083) phase [10,13,16,31,37,38]. Concomitantly, after sintering the diffraction lines for anatase TiO_2 and berlinite $AlPO_4$ disappear. In order to study, the structural changes in the composite during sintering, the high temperature X-ray diffractometry (HTXRD) was performed. The most pronounced changes in phase composition were observed around 700 °C. At that temperature, the peaks assigned to TiO_2 (anatase) and $AlPO_4$ (berlinite) started to diminish, while the lines attributed to $LiTiPO_5$ emerged (see Fig. S1 in a supplementary file). It should also be mentioned that no diffraction lines from the LBO additive were found. It is likely that no crystalline lithium borate phase was formed during sintering, at least in a detectable amount. The HTXRD results seem to indicate that at high temperatures TiO_2 and $AlPO_4$ phases react with LATP or LBO resulting in the formation of $LiTiPO_5$.

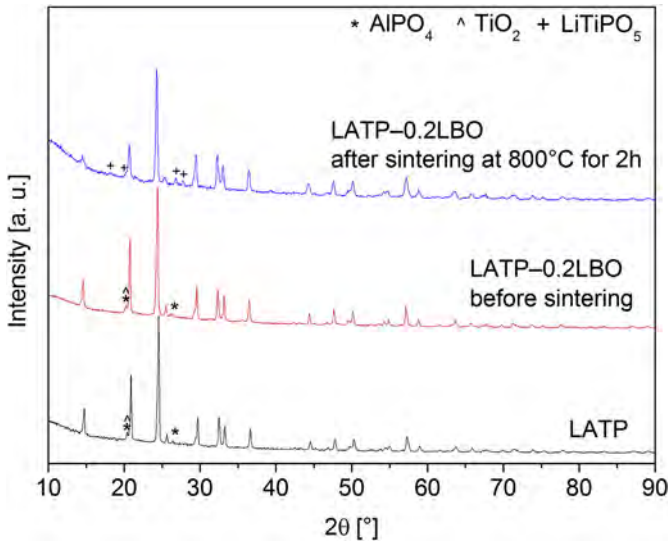

Fig. 1. XRD patterns of the as-prepared LATP and the LATP–0.2LBO composite before and after sintering at 900 °C.

3.2. Thermal analysis

Fig. 2 illustrates the thermogravimetry results for the non–sintered composites. Regardless of the composition, the highest mass loss, ca. 2 wt% occurs up to about 350 °C. This loss is probably due to the evaporation of moisture and residual ethanol present at the grain boundaries. DTA studies of LATP–LBO samples do not reveal any thermal events up to 900 °C because the content of LBO component is too low to be detected by this method. For that reason, DTA curve for LBO glass was registered separately and revealed the glass transition at T_g = 360 °C, two crystallization peaks at T_{c1} = 420 °C and at T_{c2} = 500 °C as well as the melting point at T_m = 735 °C. More detailed discussion of the DTA results for LBO glass can be found in Ref. [37]. It should be noted, that the evaluation of the glass melting point is crucial for this study as it defines the lowest possible temperature at which the LATP–LBO composites may be sintered. As discussed in the introduction part, the main role of LBO as a sintering aid is to crystallize and melt, so that its liquid phase can efficiently fill in the pores between LATP grains, providing their better mechanical contact.

3.3. Microstructure and apparent density

The impact of LBO glass on the composite microstructure was investigated on the basis of SEM images of freshly fractured pellets of: LATP sintered at 900 °C (Fig. 3A) and LATP–0.1LBO composites annealed at 700 °C (Figs. 3B), 800 °C (Figs. 3C) and 900 °C (Fig. 3D). The microstructure of sintered LATP is visibly nonuniform and composed of small grains of ca. 1 μm in size and bigger ones of a few micrometers in diameter. Also, one can discern some voids and grain boundaries between the neighboring grains. As for the composite sintered at 700 °C (Fig. 3B), the microstructure is highly porous but characterized by a more uniform grain size distribution. For LATP–0.1LBO sintered at 800 °C the microstructure is much more compact and uniform because the neighboring grains adhere better to one another. In addition, slight grain growth and almost no porosity are evidenced. Finally, in the case of the composite sintered at 900 °C, apart from grains of ca. 1 μm in size, larger ones (ca. 3 μm in size) are also observed. In addition, low concentration of bigger pores could be noticed. SEM images prove that the grain growth during sintering is induced not only by high processing temperatures but also by the presence of LBO component. After

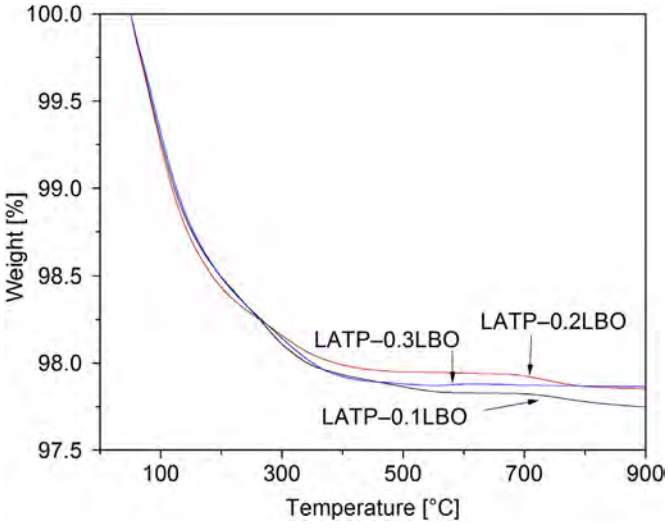

Fig. 2. TG traces for LATP–LBO composites.

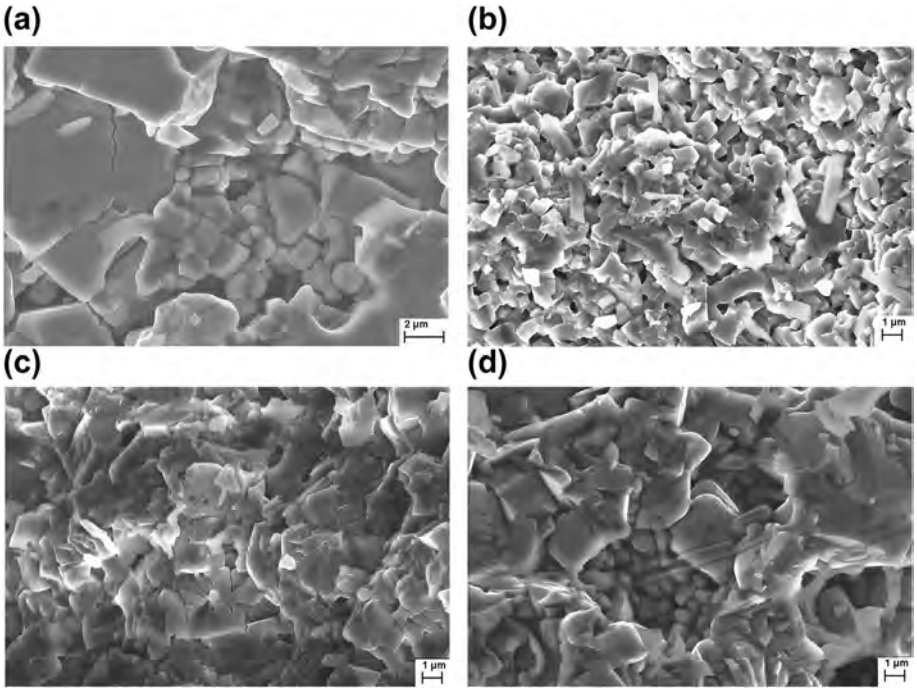

Fig. 3. SEM images of the LATP pellet sintered at 900 °C (A) and LATP−0.1LBO composite sintered at: 700 °C (B), 800 °C (C), 900 °C (D).

melting, this additive may additionally facilitate the transport of mass at grain boundaries in LATP−LBO systems.

Table 1 presents the apparent density values calculated for LATP and LATP−LBO composites. As one can notice, those values are very similar. Analysis of the collected data suggests that LBO concentration in the composite has a negligible impact on its apparent density, whereas it is the sintering temperature that plays the predominant role in the densification process. The highest density was found for LATP−LBO composites sintered at 800 °C. It is consistent with SEM studies showing that at that temperature the most compact microstructure is formed.

3.4. MAS NMR

The $^{6}Li/^{7}Li$, ^{11}B, ^{27}Al and ^{31}P MAS NMR studies were carried out on LATP base materials (non-sintered and sintered at 900 °C) and LATP−0.3LBO composites (sintered at 700, 800 or 900 °C) and supplied very accurate information about the compositional and structural changes taking place during sintering.

Table 1
Values of the apparent density of the investigated materials.

material	Sintering temperature [°C]	Apparent density [g · cm^{-3}]
LATP	700	2.69 ± 0.03
	800	2.70 ± 0.03
	900	2.71 ± 0.04
LATP−0.1LBO	700	2.64 ± 0.03
	800	2.71 ± 0.04
	900	2.63 ± 0.03
LATP−0.2LBO	700	2.63 ± 0.03
	800	2.71 ± 0.04
	900	2.67 ± 0.03
LATP−0.3LBO	700	2.64 ± 0.03
	800	2.71 ± 0.04
	900	2.66 ± 0.03

3.4.1. ^{27}Al MAS NMR

In the ^{27}Al MAS NMR spectrum of the non-sintered LATP material, five signals are observed at: −16, −15, 13, 30 and 40 ppm (Fig. 4). Signals at −16 and −15 ppm were attributed to ^{27}Al atoms in octahedral coordination (AlO_6). The peaks at 13 and 30 ppm correspond to pentahedral (AlO_5) and that at 40 ppm to tetrahedral (AlO_4) aluminum [10,15,16,27,46,47]. The peak at 40 ppm is characteristic for $AlPO_4$ [15,27], also detected in polycrystalline sample by X−ray diffraction (XRD) method. ^{27}Al signals at −16 and −15 ppm were associated with the $Li_{1+x}Al_xTi_{2-x}(PO_4)_3$ phase, where MO_6 octahedra can be occupied by M = Al or Ti [10,16,46,47]. Finally, signals at 13 and 30 ppm were ascribed to some amorphous phases containing Al^{3+} ions. The ^{27}Al NMR spectrum for LATP sample sintered at 900 °C is considerably different from the spectrum of the non-sintered base material. Although the 40 ppm line remains unchanged, the signal at 13 ppm, associated with AlO_5, decreases considerably. Simultaneously, the resonance at −15 ppm (AlO_6) of the NASICON−type phase increases significantly after heat treatment. This indicates that the Al^{3+} content of LATP crystallites increases at the expense of secondary amorphous phases during sintering.

^{27}Al MAS NMR spectrum for LATP−0.3LBO sintered at 700 °C reveals a weak signal at 40 ppm ascribed to $AlPO_4$ phase. It is worthy to note, that the lines at 30 ppm and 13 ppm, previously assigned to AlO_5 in some amorphous phases, nearly vanished which may suggest that the addition of LBO as sintering agent prevents the formation of unwanted secondary phases in LATP ceramics. Apart from signals at −16 and −15 ppm (octahedral coordination of ^{27}Al atoms), there is also a new resonance at −21 ppm. According to the literature, it may be ascribed to aluminum in octahedral coordination in $LiAlP_2O_7$ phase [48]. Analysis of ^{27}Al MAS NMR spectra for LATP−0.3LBO sintered at 800 °C and 900 °C shows that the heat treatment at temperatures higher than 700 °C promotes the formation of ^{27}Al octahedral environments characteristic for NASICON−type phase at the expense of $LiAlP_2O_7$ secondary phase.

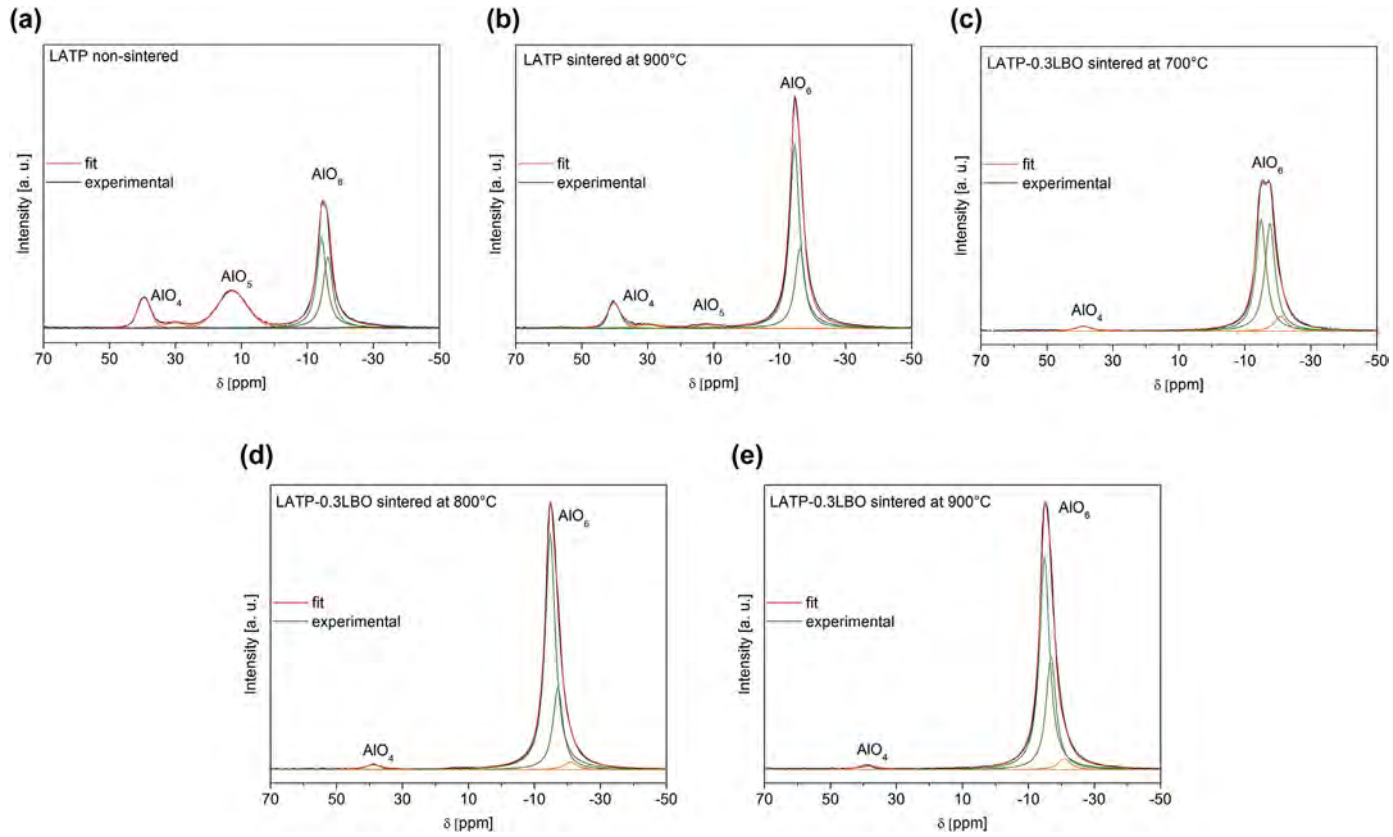

Fig. 4. ^{27}Al MAS NMR spectra of LATP non-sintered and sintered at 900 °C as well as LATP–0.3LBO non-sintered and sintered at 700, 800 or 900 °C. The experimental and simulated spectra are displayed as black and red lines, respectively. The simulated spectra are the sum of distinct lineshapes displayed as green and orange lines. (For interpretation of the references to colour in this figure legend, the reader is referred to the Web version of this article.)

^{27}Al MAS NMR data analysis implies that the polycrystalline as–prepared LATP material contains several secondary phases, not only the crystalline $AlPO_4$, but also some, other unidentified phases with penta- or octahedrally coordinated aluminum. It was shown that the heat treatment at high temperatures promotes the decomposition of unidentified phases and facilitates the transfer of Al^{3+} ions to the LATP crystal lattice. However, even after sintering at 900 °C, the decomposition is not complete and low amounts of these foreign phases still remain. The addition of LBO to LATP with subsequent heat treatment, favors the elimination of secondary phases and incorporation of Al^{3+} into the NASICON–type phase. It should be noted that the concentration of Al^{3+} in LATP is above 94% after sintering at 800 or 900 °C (see Table S1). According to the collected data, very low amount of foreign phases, $AlPO_4$ and $LiAlP_2O_7$, are still present in sintered composite. The high processing temperature as well as the presence of the LBO glass as sintering aid is believed to cause some chemical reactions within the composite at grain boundaries that release the aluminum ions from secondary phases and facilitate their incorporation into the LATP crystal structure.

3.4.2. ^{31}P MAS NMR

Fig. 5 shows the ^{31}P MAS NMR spectrum obtained for the as-prepared LATP which is dominated by one asymmetric peak at −27.5 ppm. It may be deconvoluted into six overlapped signals at: −29.3, −27.6, −27.3, −26.6, −25.9 and −24.9 ppm [6,10,16,45]. The weak resonance at −29.3 ppm may be assigned to $AlPO_4$ [6,10]. The −27.6 ppm line corresponds to the $P(OTi)_4$ environment of $LiTi_2(PO_4)_3$ phase, while the remaining peaks can be attributed to $P(OTi)_4$, $P(OTi)_3(OAl)_1$, $P(OTi)_2(OAl)_2$ and $P(OTi)_1(OAl)_3$ components of the Al–doped NASICON–type phase, where Ti^{4+} ions are partially substituted by Al^{3+}. For the sintered LATP material, the thorough spectrum deconvolution reveals a slight shift of ^{31}P signals assigned to the LATP phase towards more positive values. A comparison of relative signal intensities for $P(OTi)_{4-n}(OAl)_n$ (n = 0, 1, 2 and 3) bands between as–obtained and sintered LATP samples shows that the $P(OTi)_4$ signal at −27.6 ppm decreases at the expense of the other phosphorus coordinations $P(OTi)_{4-n}(OAl)_n$ where n = 1 and 2. That result may suggest an important transfer of Al^{3+} ions to the NASICON structure takes place upon sintering.

Further changes in ^{31}P MAS NMR spectra are observed when LATP–LBO composites are heat treated (Fig. 5). For the LATP–0.3LBO material sintered at 700 °C, the following lines can be discerned after deconvolution: −30.3, −27.7, −27.2, −26.1, −25.0, −23.9, −22.5, −9.8 and 9.8 ppm. The weak signal at −30.3 ppm is assigned to $AlPO_4$. The resonance at −27.7 ppm is attributed to the phosphorus $P(OTi)_4$ environment in the $LiTi_2(PO_4)_3$ compound. The lines in −27.2, −26.1, −25.0 and −23.9 ppm correspond to the phosphorus environments $P(OTi)_{4-n}(OAl)_n$, (where n = 0, 1, 2, 3) of the LATP phase. Finally, the signals at −22.5, −9.8 and 9.8 ppm should be assigned to newly formed lithium ion conductors, $LiAlP_2O_7$, $LiTiPO_5$ and Li_3PO_4 respectively [16,48,49]. It should be noted that the presence of the $LiTiPO_5$ phase has been also confirmed by XRD studies. Another important remark is that the concentration of $P(OTi)_4$ coordinations typical for LTP and LATP phases decrease in comparison to sintered LATP which may indicate that some part of NASICON–type phase decomposes to form other lithium ion conducting phosphates ($LiAlP_2O_7$, $LiTiPO_5$ and Li_3PO_4).

Deconvolution of ^{31}P MAS NMR spectra for LATP–LBO

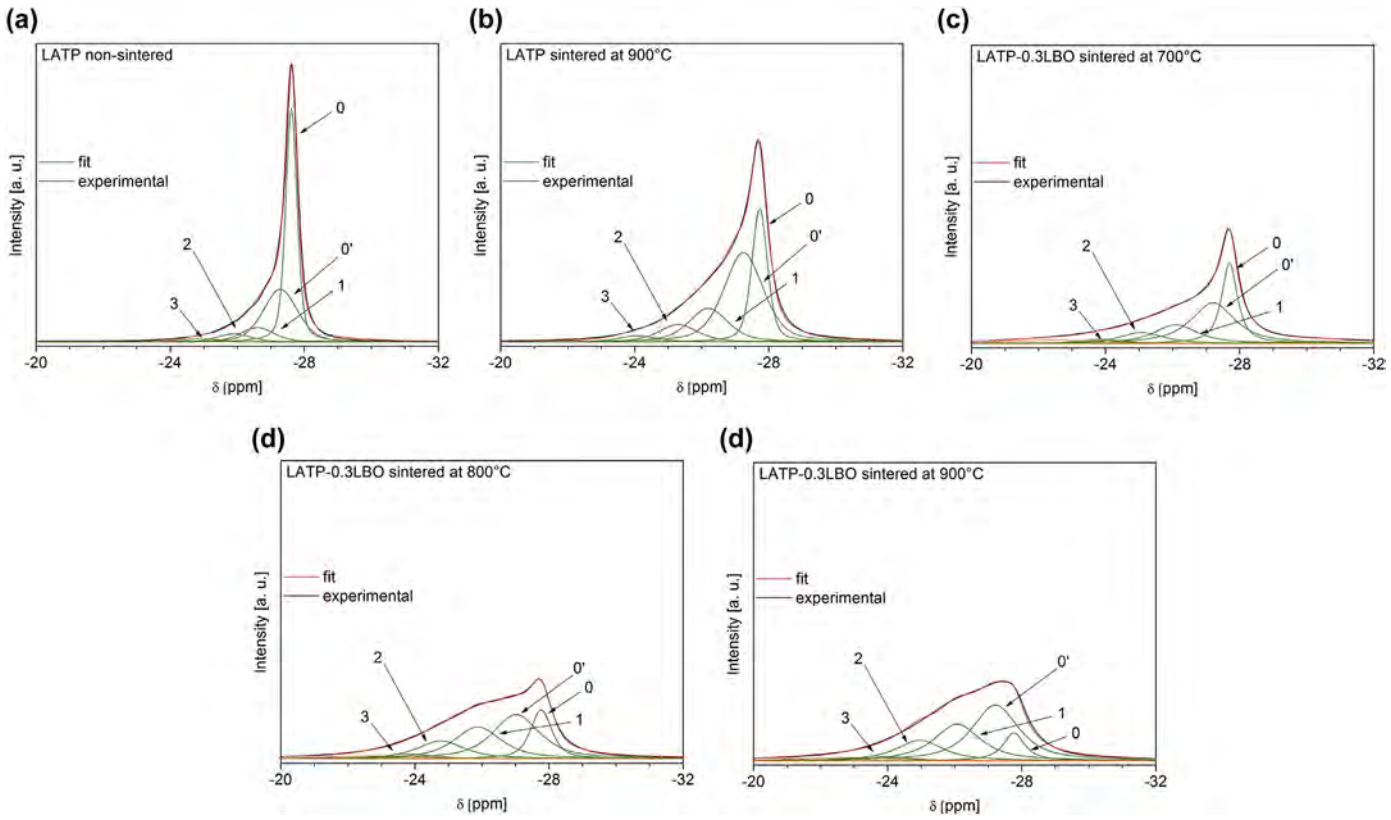

Fig. 5. ^{31}P MAS NMR spectra for LATP non-sintered and sintered at 900 °C as well as LATP–0.3LBO non-sintered and sintered at 700, 800 or 900 °C. The experimental and simulated spectra are displayed as black and red lines, respectively. The simulated spectra is the sum of distinct lineshapes displayed as green and orange lines. Numbers n = 0–4 stands for $P(OTi)_{4-n}(OAl)_n$ sites in LATP, 0′ for $P(OTi)_4$ site in LTP. (For interpretation of the references to colour in this figure legend, the reader is referred to the Web version of this article.)

composites sintered at 800 and 900 °C basically shows the same signals as for sintered LATP–LBO sintered at 700 °C. The relative signal intensity of phosphorus from impurity phases is insignificantly lower than in composite sintered at 700 °C. However, in the case of the ^{31}P signal assigned to NASICON–type phase as the sintering temperature increases, the relative $P(OTi)_4$ signal intensity at −27.7 ppm (for LTP phase) decreases, while the one for $P(OTi)_3(OAl)_1$ (−26.1 ppm) as well as for $P(OTi)_2(OAl)_2$ (−25.0 ppm) increases. That may be another argument supporting the claim that Al^{3+} ions may diffuse from grain boundaries to incorporate into the LATP crystal lattice.

The ^{27}Al MAS NMR studies described in the previous section led to the conclusion that the heat treatment is likely to provoke the diffusion of aluminum ions into the LATP structure. Now, ^{31}P MAS NMR investigations brings complementary information concerning this process. It has been proved that the sintering of the base material diminishes the concentration of $P(OTi)_4$ tetrahedrons, which might be related to the diffusion of Al^{3+} ions from foreign phases into the LATP structure. Some of those ions might substitute for titanium ions, increasing the concentration of $P(OTi)_3(OAl)_1$ and $P(OTi)_2(OAl)_2$ phosphorus coordinations. The concentration of Al^{3+} ions in respect to Ti^{4+} ions could be deduced using the following expression [6,10]:

$$\frac{Al^{3+}}{Ti^{4+}} = \frac{4I_4 + 3I_3 + 2I_2 + I_1}{4I_0 + 3I_1 + 2I_2 + I_3} = \frac{x}{2-x} \quad (1)$$

where I_n (n = 0, 1, 2, 3 and 4) stands for the relative signal intensity of ^{31}P bands associated with $P(OTi)_{4-n}(OAl)_n$ environments. Based on Eq. (1), the nominal and actual Al^{3+} concentrations for LATP phase were compared for different composites and are presented in Table S2. It can be seen that the aluminum content in LATP phase approaches the nominal value for the sintering temperature equal to 800 °C. Those results strongly suggest (in agreement with ^{27}Al MAS NMR results) that the heat treatment of LATP–LBO composites favors the incorporation of Al^{3+} into the NASICON–type phase.

3.4.3. ^{6}Li MAS NMR

Fig. 6 presents the ^{6}Li (I = 1) MAS NMR spectra for pristine and sintered LATP material. As a consequence of small dipolar and quadrupolar interactions, only central (CT) transitions of ^{6}Li MAS NMR spectra were detected. Simulation of the spectrum for the as–prepared LATP sample reveals the presence of two peaks, one at −1.1 and the other at −0.7 ppm, which can be assigned to lithium in Li1 and Li3 sites in the NASICON crystal structure [10,45,46]. The integrated signal intensity at −1.1 ppm is three times higher than at −0.7 ppm. In the sintered LATP compound, the similar peaks were detected. However, it should be emphasized that their integrated intensity changed significantly with respect to as–obtained LATP. After sintering, the signal ascribed to Li3 site is much more intense than that for Li1 site. Based on these observations, it might be concluded that the incorporation of Al^{3+} ions upon sintering promotes the occupation of Li3 sites by lithium ions.

As for the sintered LATP–LBO composites, two peaks at −1.1 and −0.7 ppm are still observed. Moreover, with increasing sintering temperature the integrated intensity of Li3 site increases when compared to Li1 site. It may suggest, that Li3 sites becomes the preferred one for Li^+ ions. Also, two additional peaks were detected at −0.3 and 0 ppm, that most probably should be attributed to the lithium borate and $LiTiPO_5$ secondary phase, respectively. For the

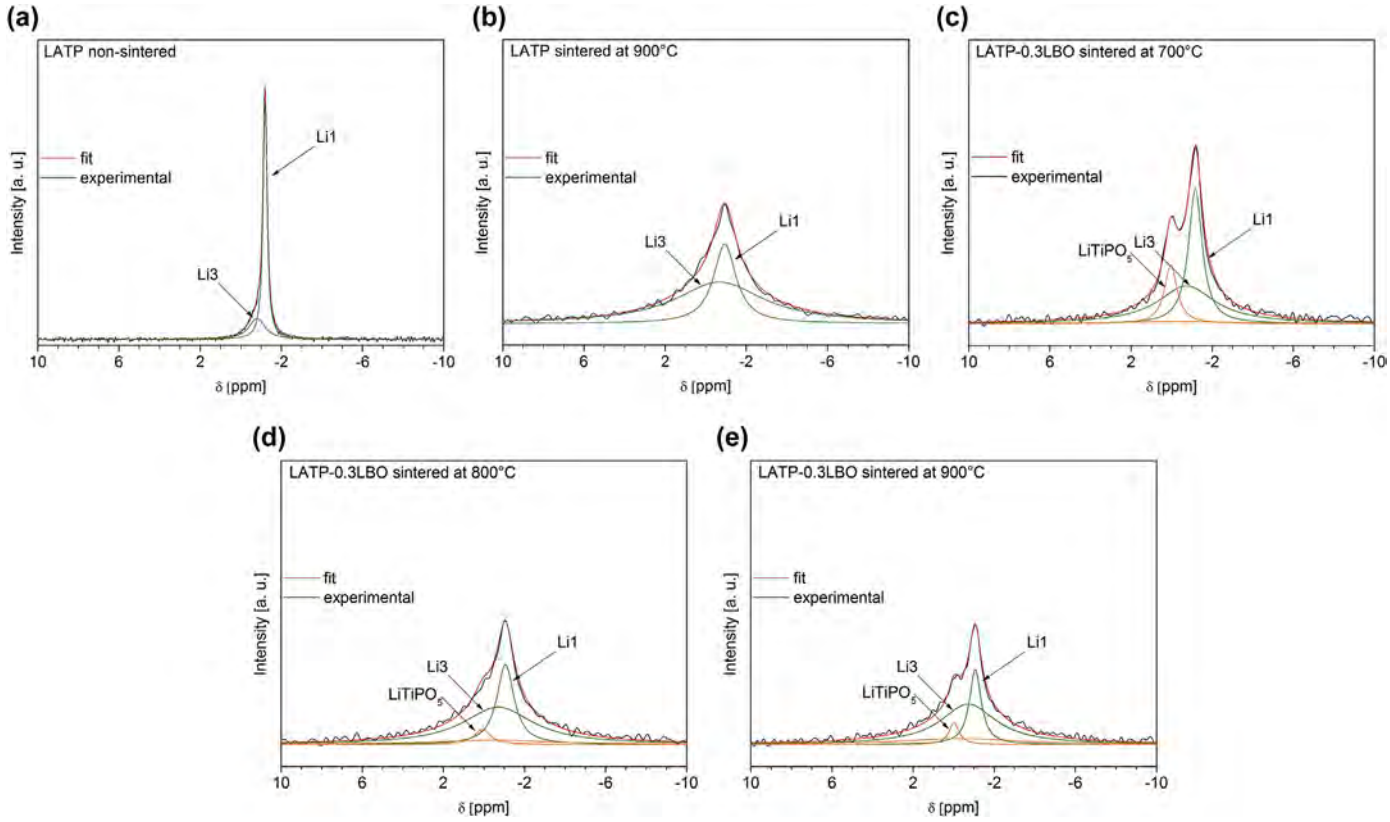

Fig. 6. ^{6}Li NMR spectra for LATP non-sintered and sintered at 900 °C as well as LATP−0.3LBO non-sintered and sintered at 700, 800 or 900 °C. The experimental and simulated spectra are displayed as black and red lines, respectively. The simulated spectra are the sum of distinct lineshapes displayed as green and orange lines. The different sites of LATP are labeled Li1 and Li3. The spectra of the five samples are displayed with identical intensity scales. (For interpretation of the references to colour in this figure legend, the reader is referred to the Web version of this article.)

composite sintered at 700 °C, the relative integrated intensity of the signals shows that there is apparently more lithium ions in $LiTiPO_5$ phase than in lithium borate. However, when the composites are sintered at 800 or 900 °C, the ratio of Li^+ concentration in those phases reverses. What is more, the content of lithium ions in phases other than LATP is almost the same, regardless of the sintering temperature. In addition, the heat treatment process broadens the ^{6}Li NMR signals for both, Li1 and Li3 sites, indicating that exchange between both sites increases after sintering.

The temperature dependent ^{6}Li MAS NMR spectroscopy was performed for the composite material sintered at 800 °C. Generally, the obtained spectra become narrower with increasing temperature. Deconvolution of the spectra revealed significant changes in occupation of Li ions of Li1 and Li3 sites. The relative integrated intensity of the signal assigned to Li1 site increases while the one for Li3 site decreases with increasing temperature. However, the total concentration of lithium ions in NASICON−type phase remains almost the same, regardless the temperature. As for the concentration of Li^+ in secondary phases, the relative integrated intensity of the signal attributed to $LiTiPO_5$ increases at 80 °C, while the one assigned to lithium borate decreases. Heating the sample up to 150 °C does not lead to any significant changes in lithium environments in these phases. After cooling to room temperature the spectrum returns to its original shape.

3.4.4. ^{7}Li MAS NMR

^{7}Li (I = 3/2) MAS NMR spectra for LATP and LATP−LBO samples are presented in Fig. 7. The analysis of quadropolar interactions is supposed to provide some information about the sites symmetry, while the linewidth evolution can be associated with changes in the mobility of lithium ions. The deconvolution of ^{7}Li MAS NMR central transitions reveals the presence of the same components that have been already detected in the case of ^{6}Li MAS NMR. For the non−sintered LATP, the spectra consists of two overlapping lines at −1.2 and −0.9 ppm with quadrupolar coupling constant (C_Q) assigned to Li1 (38 kHz) and Li3 (80 kHz) sites in NASICON crystal structure [10,16,45–47]. The relative integrated intensity of the Li1 line is higher than for the Li3 signal. As for the sintered LATP, one can notice lower C_Q values, equal 23 and 52 kHz for Li1 and Li3 sites respectively. The decrease in C_Q values may be explained by the substitution of Ti^{4+} by Al^{3+} ions in the NASICON structure, resulting in the increase of lithium mobility. Moreover, the ^{7}Li NMR signal for sintered samples is visibly broader than for non-sintered ones suggesting different arrangement of Li^+ ions. Similarly as in the case of ^{6}Li MAS NMR spectra, the relative integrated intensity of Li3 site signal is higher than for Li1 site.

Analysis of the ^{7}Li MAS NMR spectra for LATP−LBO composites indicates that the preferred site for lithium ions is Li3, regardless of the sintering temperature. For composite sintered at 700 °C the quadrupolar coupling constants are equal to 40 and 69 kHz for Li1 and Li3 site respectively. The higher the sintering temperature, the lower the C_Q values for both lithium sites. Deconvolution of those spectra shows the presence of two additional signals at −0.3 and 0 ppm assigned to lithium borate and $LiTiPO_5$ phases. It should be noted that the spectra obtained in the ^{7}Li MAS NMR experiment had lower resolution as compared to ^{6}Li MAS NMR data. Despite this limitation, they proved their usefulness as they enabled us to perform the complementary analysis in terms of quadrupolar parameters for all signal components.

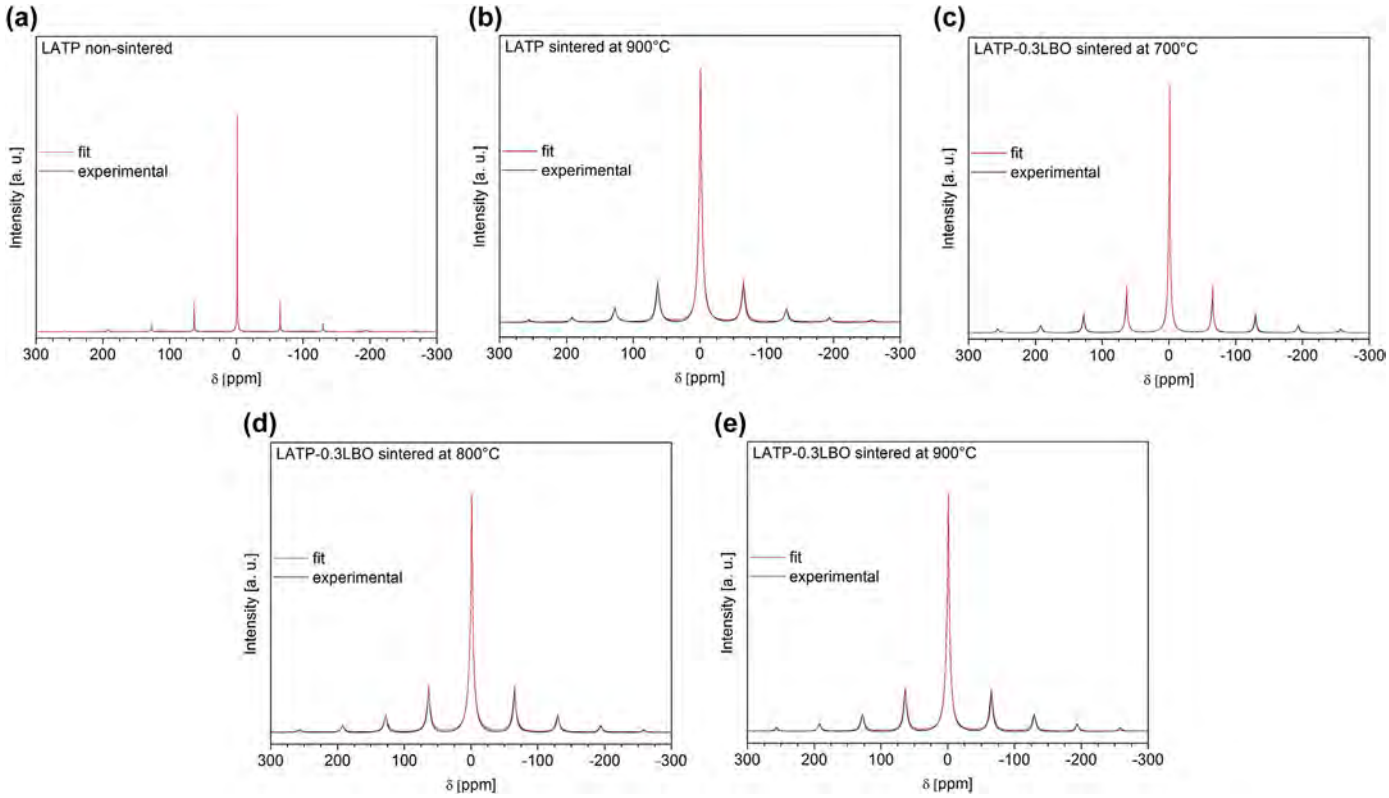

Fig. 7. CT (central transition) of ^{7}Li NMR spectra under MAS conditions of LATP non-sintered and sintered at 900 °C as well as LATP–0.3LBO non-sintered and sintered at 700, 800 or 900 °C. The experimental and simulated spectra are displayed as black and red lines, respectively. (For interpretation of the references to colour in this figure legend, the reader is referred to the Web version of this article.)

3.4.5. ^{7}Li PFG NMR

The ^{7}Li PFG NMR analysis of LATP and LATP–LBO samples reveals that only the pristine LATP sample display long T2 values to perform PFG measurements. Based on those results the Li^{+} diffusion coefficient for non-sintered LATP was found to be equal to ca. 9×10^{-12} m^2/s. Unfortunately, for the ceramic samples Li exchange processes enlarged the linewidth of the ^{7}Li echo signals to such extend that their detection was no longer possible.

3.4.6. ^{11}B MAS NMR

Fig. 8 presents the ^{11}B MAS NMR spectra for the LATP–LBO composites sintered at 700, 800 or 900 °C. The spectrum for the composite sintered at 700 °C consists of two lines located at 8.1 and −1.8 ppm, which are ascribed to BO_3 and BO_4 environments, respectively. Both BO_3 and BO_4 signals could be simulated using two lineshapes. So that, the former one could be represented by two peaks resonating at 8.3 and 3.0 ppm. As for the BO_4 coordination, two signals at −1.6 and −3.6 ppm were found. Higher relative integrated intensity of the signal centered at −1.8 ppm suggests that BO_4 environment is predominant in the studied samples. It is worth mentioning that the ^{11}B MAS NMR spectra for composites sintered at different temperatures are quite similar. It follows that only small structural changes occur to boron environment during heat treatment at high temperatures.

3.5. Impedance spectroscopy

The impedance spectroscopy results are presented in Figs. 9 and 10. Two exemplary Nyquist plots collected at 30 °C for LATP sintered at 900 °C and LATP–0.3LBO composite annealed at 700 °C are shown on Fig. 9. The first one consists of a small semicircle at high frequencies, almost regular semicircle at intermediate frequencies followed by a spur at lower frequencies. The shape of the spectrum suggests that electrical properties of the ceramic LATP can be modelled by an electrical circuit composed of two loops connected in series, each containing a resistor R shunted by a constant phase element CPE. The first loop (at higher frequencies) represents the grain interior and the second one (at lower frequencies) – the grain boundary region. The total and apparent grain conductivity can be evaluated using the formula $\sigma = L/(R{\cdot}A)$, where L and A stand for the sample thickness and electrode area. The values of R_{gr} and $R_{tot} = R_{gr} + R_{gb}$ can be derived from the intersection of each circle with Re Z axis. Because the precise geometrical factor of the grains and grain boundary thickness are not known, in this study conductivity values derived from IS experiment are referred to as *apparent* ones. In the case of LATP sintered at 900 °C, the total conductivity σ_{tot} equals ca. 4.7×10^{-5} $S \cdot cm^{-1}$.

When LBO glass is added to the LATP base matrix and sintered at high temperatures, the significant enhancement of the electrical properties is observed. For the composites under study, the Nyquist plots exhibit two semicircles followed by a spur. For that reason the electrical properties of the composite were analyzed in a similar way that in the case of sintered LATP. The estimated values of the total, apparent grain and grain boundaries conductivities are given in Table 2. It is worth noting that the composites with the most compact microstructure, i.e. those sintered at 800 °C also exhibited the best ionic conductivity.

From the temperature dependent IS measurements it was concluded that the total ionic conductivity for LATP–LBO composites fulfills Arrhenius dependence with a single activation energy (Fig. 10), regardless the sintering temperature and composition. The activation energy for the total (E_{tot}) and grain (E_{gr})

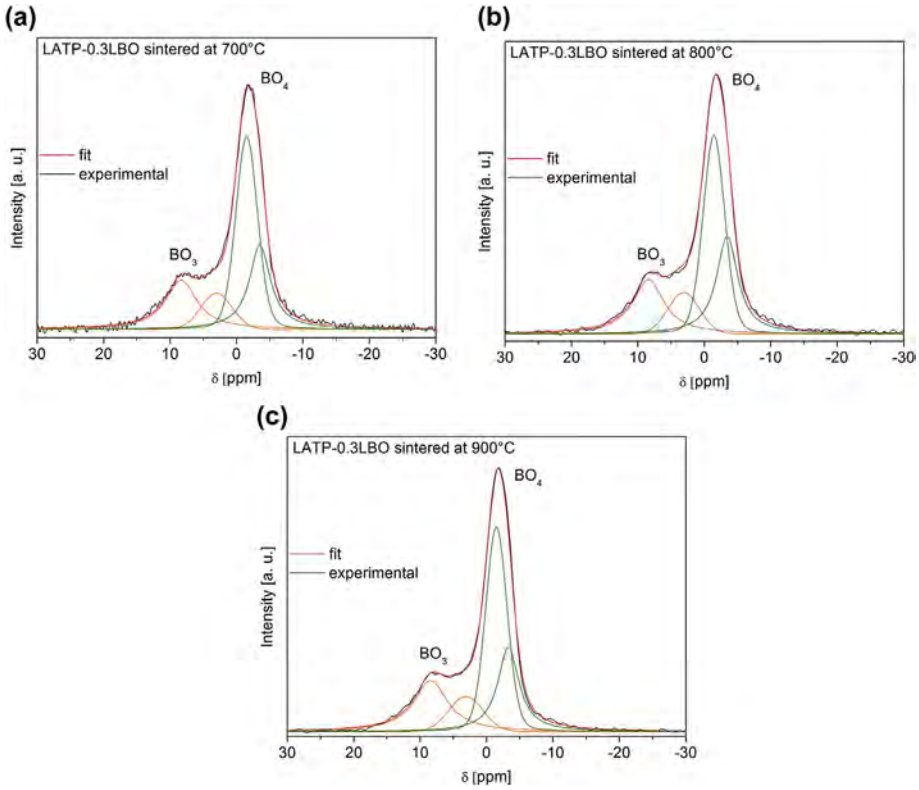

Fig. 8. ^{11}B MAS NMR spectra of LATP−0.3LBO sintered at 700, 800 or 900 °C. The experimental and simulated spectra are displayed as black and red lines, respectively. The simulated spectra are the sum of distinct lineshapes displayed as green and orange lines. (For interpretation of the references to colour in this figure legend, the reader is referred to the Web version of this article.)

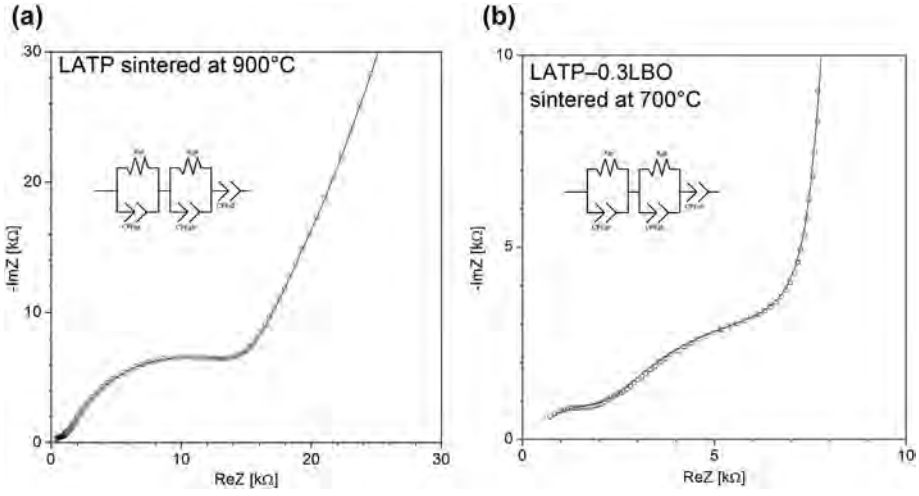

Fig. 9. Nyquist plots for the data collected at 30 °C for (A) LATP ceramic sintered at 900 °C and (B) LATP−0.1LBO composite sintered at 700 °C. The equivalent circuits modeling the electrical properties of the sintered materials are displayed as insets.

conductivity does not depend on the LBO content (Table 2) for composites sintered at a given temperature. In addition, the values of *Etot* are relatively higher for samples sintered at 900 °C (0.35 eV) than for materials annealed at 700 °C and 800 °C (ca. 0.31 eV). For grain interiors, the activation energy (*Egr*) equals to 0.20 eV, regardless of the composition and sintering temperature. The presented results are consistent with the literature reports, where the total activation energy varies in the range from 0.2 to 0.4 eV, while for the grains, it is in the range from 0.2 to 0.3 eV [10,13,15,17,20,23,26–28,32,36,45].

The changes in ionic conductivity for the materials under study may be analyzed in terms of the brick layer model (BLM) [47,50–54]. In this model the ceramic material is represented by a system of adjacent cubes of size *D*, each coated with a thin layer of thickness *d*. Assuming that cubes correspond to LATP grains and the thin layer between them to the grain boundary region, the total conductivity, σ_{tot} could be expressed as follows [47]:

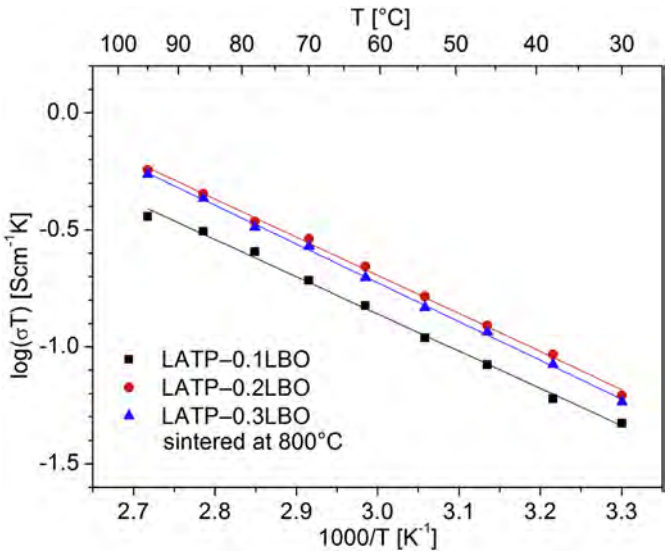

Fig. 10. Arrhenius plots of the total electric conductivity of the LATP–LBO composites sintered at 800 °C.

$$\sigma_{\mathrm{tot}} = \frac{(1-2\alpha)^2\sigma_{\mathrm{gr}}}{(1-2\alpha)+2\alpha\frac{\sigma_{\mathrm{gr}}}{\sigma_{\mathrm{gb}}}} + 4\alpha(1-\alpha)\sigma_{\mathrm{gb}} \quad (2)$$

where, $\alpha = d/D$ and, σ_{gr} and σ_{gb} denote the true grain and grain boundary conductivity values but not the apparent ones (determined by means of impedance spectroscopy). If the conductivity of the grain boundary region is much lower than the conductivity of the bulk, i.e. $\sigma_{gr} \gg \sigma_{gb}$, then the formula can be simplified into:

$$\sigma_{\mathrm{tot}} \approx \left[\frac{(1-2\alpha)^2}{2\alpha} + 4\alpha(1-\alpha)\right]\sigma_{\mathrm{gb}} \quad (3)$$

In that case, the electrical properties are limited by the conductivity of the grain boundary phase and the size of the grains and grain boundary layer. As–prepared and ceramic LATP as well as non–sintered composite meet that criterion, with $\sigma_{gr} > 10\sigma_{gb}$. The XRD and MAS NMR data analysis confirms the presence of poorly conducting secondary phases ($AlPO_4$, glassy ones containing Al^{3+} and TiO_2) located at grain boundaries. The transport of Li^+ ions is then hindered by those foreign phases and, as a consequence, the total ionic conductivity is relatively low. Sintering of LATP material results in its densification and decomposition of glassy phase containing Al^{3+} ions. As a result, its total ionic conductivity is higher than for non–sintered material, but it still remains low because of the presence of $AlPO_4$ phase.

A complete decomposition of poorly conducting phases, including $AlPO_4$ may be achieved when LBO is added to LATP matrix and then sintered at high temperatures. Then, the formation of lithium ion conducting phases, such as $LiAlP_2O_7$, $LiTiPO_5$ and Li_3PO_4 takes place. As a result, the grain boundaries conductivity significantly increases (Table 2). With respect to the ceramic LATP, values of σ_{gb} for LATP–LBO composites are about one order of magnitude higher. One can notice, that for the sintered composites, value of the total ionic conductivity is only four times lower than the bulk conductivity. Also, as shown by SEM studies, the addition of LBO affects the material microstructure – the grain contact is improved and porosity reduced. Therefore, in such a case, the grain boundary layer is thin in comparison to grain size ($\alpha \ll 1$) and under this assumption Eq. (2) transforms into:

$$\sigma_{\mathrm{tot}} = \frac{\sigma_{\mathrm{gr}}}{1+2\alpha\frac{\sigma_{\mathrm{gr}}}{\sigma_{\mathrm{gb}}}} \quad (4)$$

One can observe that if $\alpha\sigma_{gr}/\sigma_{gb} \ll 1$, i.e. grains are large and σ_{gb} is comparable to σ_{gr}, the model predicts that $\sigma_{tot} \approx \sigma_{gr}$.

From the above analysis carried out in terms of the BLM and Eqs. (2)–(4), we suggest that the enhancement of total ionic conductivity in LATP–LBO composites could be caused by at least two factors. First one is related to the microstructure changes (densification and grain growth) during sintering. The other one is the decomposition of highly resistant phases at the grain boundaries caused by the sintering of LATP with LBO additive. These two factors may simultaneously influence the total ionic conductivity, as sintering with the presence of LBO not only modifies the microstructure but also changes the phase composition of the grains and grain boundary region.

In general, XRD and NMR studies show that the non–sintered LATP contains not only the NASICON–type phase but also some other unwanted, insulating compounds. Therefore, the concentration of Al^{3+} ions in NASICON–type phase should be lower than expected. The sintering of LATP with LBO leads to the formation of grains with chemical formula closer to the assumed one. The subsequent stages of this process may as follows (Fig. 11):

1) decomposition of the insulating grain boundary phases at high temperatures with subsequent release of the aluminum ions,
2) substitution of Ti^{4+} by Al^{3+} in the NASICON–type crystal lattice,
3) backward diffusion of the released titanium ions to the grain surface,

Table 2
Values of bulk (σ_{gr}), grain boundary (σ_{gb}) and total (σ_{tot}) ionic conductivities at 30 °C as well as the bulk (E_{gr}) and total (E_{tot}) activation energies.

material	T_{sint} [°C]	σ_{gr} (30 °C) [S · cm^{-1}]	σ_{gb} (30 °C) [S · cm^{-1}]	σ_{tot} (30 °C) [S · cm^{-1}]	E_{gr} [eV]	E_{tot} [eV]
LATP	700	8.8×10^{-5}	2.0×10^{-6}	1.9×10^{-6}	0.21	0.46
	800	2.0×10^{-4}	1.1×10^{-5}	1.0×10^{-5}	0.21	0.39
	900	5.1×10^{-4}	5.4×10^{-5}	4.7×10^{-5}	0.21	0.40
LATP–0.1LBO	700	3.9×10^{-4}	1.8×10^{-4}	1.2×10^{-4}	0.19	0.30
	800	6.7×10^{-4}	3.0×10^{-4}	2.1×10^{-4}	0.20	0.32
	900	3.0×10^{-4}	0.7×10^{-4}	0.6×10^{-4}	0.21	0.35
LATP–0.2LBO	700	3.3×10^{-4}	1.1×10^{-4}	0.8×10^{-4}	0.19	0.30
	800	7.4×10^{-4}	2.6×10^{-4}	1.9×10^{-4}	0.21	0.32
	900	3.9×10^{-4}	1.2×10^{-4}	0.9×10^{-4}	0.21	0.35
LATP–0.3LBO	700	3.0×10^{-4}	0.9×10^{-4}	0.7×10^{-4}	0.19	0.30
	800	5.7×10^{-4}	2.2×10^{-4}	1.6×10^{-4}	0.20	0.32
	900	3.9×10^{-4}	1.2×10^{-4}	0.9×10^{-4}	0.21	0.35

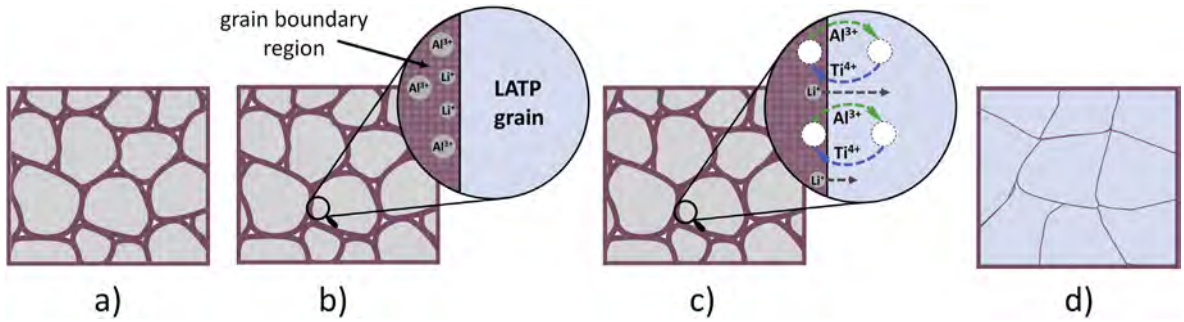

Fig. 11. Illustration of the sintering mechanism proposed for LATP–LBO composites: a) microstructure before sintering, b) release of Al^{3+} ions due to the decomposition of secondary phases at high temperatures, c) migration of Al^{3+} and Li^{+} towards LATP grains and their incorporation into the crystalline lattice; diffusion of Ti^{4+} towards grain boundaries followed by the formation of new phases there, d) microstructure after sintering.

4) reaction of titanium ions at grain boundaries followed by the formation of secondary phases supporting the lithium–ion transport between the grains.

So, the NMR studies suggest that the chemical composition of grains and grain boundary region may be different in each case. Therefore, different values of grain and total activation energy are observed in many literature reports [10,13,15,17,20,23,26–28,32,36,45]. As the impedance data shows, the impact of LBO additive on the total ionic conductivity depends mostly on sintering temperature. It is important to recall that the most dense material was obtained after sintering at 800 °C. Also, for that sintering temperature, LATP–LBO composites exhibit the best total, grain and grain boundaries conductivities values. Considering the combined IS and SEM results, it may be concluded that the total ionic conductivity increases most probably due to the better adhesion of neighboring LATP grains and the presence of small amounts of appropriate lithium ion conducting phases between them. In the light of presented results, the further increase of the total ionic conductivity is still possible provided that the concentration of foreign phases in composites would be further reduced.

4. Conclusions

Preparation of highly conducting ceramic solid electrolyte for all solid state lithium–ion batteries is possible when appropriate material is introduced to the base matrix and sintered at high temperature. In the case of $Li_{1.3}Al_{0.3}Ti_{1.7}(PO_4)_3$–$y$ ($0.75Li_2O \cdot 0.25B_2O_3$) ($0 \leq y \leq 0.3$) system, the experimental evidence clearly shows that the composite formation is an efficient way to synthesize material with high total ionic conductivity. In this study, we suggest that three main processes may be responsible for the enhancement of total ionic conductivity: (i) densification and better adhesion of neighboring grains, (ii) the decomposition of $AlPO_4$, TiO_2 and amorphous aluminophosphate phases at the grain boundaries and (iii) the formation of some lithium conducting phosphates in the presence of $0.75Li_2O \cdot 0.25B_2O_3$ glass. Among the studied composites, the best conducting one, LATP–0.1LBO sintered at 800 °C, exhibits the total ionic conductivity σ_{tot} equal to 2.1×10^{-4} S · cm^{-1} at room temperature, which is almost one order of magnitude higher than for the ceramic LATP. In conclusion, the ease of preparation as well as good electrical properties of the LATP–LBO composites are the main features advocating for their application as solid electrolytes in the all solid lithium–ion battery technology. The aim of our further study will be to test their performance in prototype electrochemical cells.

Declaration of competing interest

The authors declare that they have no known competing financial interests or personal relationships that could have appeared to influence the work reported in this paper.

CRediT authorship contribution statement

K. Kwatek: Conceptualization, Methodology, Validation, Formal analysis, Investigation, Resources, Writing - original draft, Writing - review & editing, Funding acquisition, Project administration. **W. Ślubowska:** Conceptualization, Methodology, Investigation, Resources, Writing - original draft, Writing - review & editing. **C. Ruiz:** Formal analysis, Investigation, Resources, Validation. **I. Sobrados:** Formal analysis, Investigation, Resources, Validation, Writing - review & editing, Project administration. **J. Sanz:** Formal analysis, Validation, Writing - review & editing, Supervision, Project administration. **J.E. Garbarczyk:** Validation, Writing - review & editing, Supervision, Funding acquisition. **J.L. Nowiński:** Conceptualization, Methodology, Validation, Writing - review & editing, Supervision.

Acknowledgments

The Polish group has received funding from “International scholarship exchange of doctoral students and academic staff” implemented as part of the Activity specified in the application for co-financing of the project no. POWR.03.03.00–00-PN13/18. The program is co-financed from the European Social Fund under the Operational Program Knowledge Education Development.

The Spanish group has received funding from the MINECO MAT2016-78362-C4-2R.

Appendix A. Supplementary data

Supplementary data to this article can be found online at https://doi.org/10.1016/j.jallcom.2020.155623.

References

[1] C. Sun, J. Liu, Y. Gong, D.P. Wilkinson, J. Zhang, Recent advances in all-solid-state rechargeable lithium batteries, Nano Energy 33 (2017) 363–386, https://doi.org/10.1016/j.nanoen.2017.01.028.
[2] F. Zheng, M. Kotobuki, S. Song, M.O. Lai, L. Lu, Review on solid electrolytes for all-solid-state lithium-ion batteries, J. Power Sources 389 (2018) 198–213, https://doi.org/10.1016/j.jpowsour.2018.04.022.
[3] K. Takada, Progress and prospective of solid-state lithium batteries, Acta Mater. 61 (2013) 759–770, https://doi.org/10.1016/j.actamat.2012.10.034.
[4] W. Xiao, J. Wang, L. Fan, J. Zhang, X. Li, Recent advances in $Li_{1+x}Al_xTi_{2-x}(PO_4)_3$ solid-state electrolyte for safe lithium batteries, Energy Storage Mater 19 (2019) 379–400, https://doi.org/10.1016/j.ensm.2018.10.012.

[5] N.F. Uvarov, A.S. Ulikhin, Y.G. Materishina, Ion conductors with the conductivity over lithium ions and solid electrochemical devices based on them, Chem. Sustain. Dev. 20 (2012) 69–76.

[6] K. Arbi, J.M. Rojo, J. Sanz, Lithium mobility in titanium based Nasicon $Li_{1+x}Ti_{2-x}Al_x(PO_4)_3$ and $LiTi_{2-x}Zr_x(PO_4)_3$ materials followed by NMR and impedance spectroscopy, J. Eur. Ceram. Soc. 27 (2007) 4215–4218, https://doi.org/10.1016/j.jeurceramsoc.2007.02.118.

[7] H. Aono, E. Sugimoto, Y. Sadaoka, N. Imanaka, G.-Y. Adachi, Ionic conductivity of solid electrolytes based on lithium titanium phosphate, J. Electrochem. Soc. 137 (1990) 1023–1027.

[8] M. Kotobuki, M. Koishi, Y. Kato, Preparation of $Li_{1.5}Al_{0.5}Ti_{1.5}(PO_4)_3$ solid electrolyte via a co-precipitation method, Ionics (Kiel) 19 (2013) 1945–1948, https://doi.org/10.1007/s11581-013-1000-4.

[9] M. Kotobuki, M. Koishi, Effect of Li salts on the properties of $Li_{1.5}Al_{0.5}Ti_{1.5}(PO_4)_3$ solid electrolytes prepared by the co-precipitation method, J. Asian Ceram. Soc. 7 (2019) 426–433, https://doi.org/10.1080/21870764.2019.1652971.

[10] K. Arbi, S. Mandal, J.M. Rojo, J. Sanz, Dependence of ionic conductivity on composition of fast ionic conductors $Li_{1+x}Ti_{2-x}Al_x(PO_4)_3$, $0 \le x \le 0.7$. A parallel NMR and electric impedance study, Chem. Mater. 14 (2002) 1091–1097, https://doi.org/10.1021/cm010528i.

[11] S. Wang, L. Ben, H. Li, L. Chen, Identifying Li^+ ion transport properties of aluminum doped lithium titanium phosphate solid electrolyte at wide temperature range, Solid State Ionics 268 (2014) 110–116, https://doi.org/10.1016/j.ssi.2014.10.004.

[12] T. Šalkus, M. Barre, A. Kežionis, E. Kazakevičius, O. Bohnke, A. Selskienė, A.F. Orliukas, Ionic conductivity of $Li_{1.3}Al_{0.3-x}Sc_xTi_{1.7}(PO_4)_3$ (x=0, 0.1, 0.15, 0.2, 0.3) solid electrolytes prepared by Pechini process, Solid State Ionics 225 (2012) 615–619, https://doi.org/10.1016/j.ssi.2012.03.045.

[13] A.F. Orliukas, T. Šalkus, A. Kežionis, A. Dindune, Z. Kanepe, J. Ronis, V. Venckutė, V. Kazlauskienė, J. Miškinis, A. Lukauskas, Structure and broadband impedance spectroscopy of $Li_{1.3}Al_yY_{x-y}Ti_{1.7}(PO_4)_3$ (x=0.3; y=0.1, 0.2) solid electrolyte ceramics, Solid State Ionics 225 (2012) 620–625, https://doi.org/10.1016/j.ssi.2012.05.011.

[14] W. Ślubowska, K. Kwatek, C. Jastrzębski, J.L. Nowiński, Thermal, structural and electrical study of boron-incorporated LATP glasses and glass-ceramics, Solid State Ionics 335 (2019) 129–134, https://doi.org/10.1016/j.ssi.2019.02.022.

[15] A.S. Best, M. Forsyth, D.R. MacFarlane, Stoichiometric changes in lithium conducting materials based on $Li_{1+x}Al_xTi_{2-x}(PO_4)_3$: impedance, X-ray and NMR studies, Solid State Ionics 136–137 (2000) 339–344, https://doi.org/10.1016/S0167-2738(00)00493-8.

[16] K. Kwatek, W. Ślubowska, J. Trébosc, O. Lafon, J.L. Nowiński, Structural and electrical properties of ceramic Li-ion conductors based on $Li_{1.3}Al_{0.3}Ti_{1.7}(PO_4)_3$-LiF, J. Eur. Ceram. Soc. 40 (2020) 85–93, https://doi.org/10.1016/j.jeurceramsoc.2019.08.032.

[17] M. Kotobuki, M. Koishi, Influence of precursor calcination temperature on sintering and conductivity of $Li_{1.5}Al_{0.5}Ti_{1.5}(PO_4)_3$ ceramics, J. Asian Ceram. Soc. 7 (2019) 69–74, https://doi.org/10.1080/21870764.2018.1564166.

[18] E. Zhao, Y. Guo, G. Xu, L. Yuan, J. Liu, X. Li, L. Yang, J. Ma, Y. Li, S. Fan, High ionic conductivity Y doped $Li_{1.3}Al_{0.3}Ti_{1.7}(PO_4)_3$ solid electrolyte, J. Alloys Compd. 782 (2019) 384–391, https://doi.org/10.1016/j.jallcom.2018.12.183.

[19] S. Ling, J. Peng, Q. Yang, J. Qiu, Enhanced ionic conductivity in LAGP/LATP composite electrolyte, Chin. Phys. B 27 (2018), 038201, https://doi.org/10.1088/1674-1056/27/3/038201.

[20] D.H. Kothari, D.K. Kanchan, Effect of doping of trivalent cations Ga^{3+}, Sc^{3+}, Y^{3+} in $Li_{1.3}Al_{0.3}Ti_{1.7}(PO_4)_3$ (LATP) system on Li+ ion conductivity, Phys. B Phys. Condens. Matter. 501 (2016) 90–94, https://doi.org/10.1016/j.physb.2016.08.020.

[21] M. Kotobuki, M. Koishi, Preparation of $Li_{1.5}Al_{0.5}Ti_{1.5}(PO_4)_3$ solid electrolyte via a sol–gel route using various Al sources, Ceram. Int. 39 (2013) 4645–4649, https://doi.org/10.1016/j.ceramint.2012.10.206.

[22] M. Kotobuki, B. Kobayashi, M. Koishi, T. Mizushima, N. Kakuta, Preparation of $Li_{1.5}Al_{0.5}Ti_{1.5}(PO_4)_3$ solid electrolyte via coprecipitation using various PO_4 sources, Mater. Technol. 29 (2014) A93–A97, https://doi.org/10.1179/1753555714Y.0000000181.

[23] C. Davis, J.C. Nino, Microwave processing for improved ionic conductivity in Li_2O-Al_2O_3-TiO_2-P_2O_5 glass-ceramics, J. Am. Ceram. Soc. 98 (2015) 2422–2427, https://doi.org/10.1111/jace.13638.

[24] K. Waetzig, A. Rost, U. Langklotz, B. Matthey, J. Schilm, An explanation of the microcrack formation in $Li_{1.3}Al_{0.3}Ti_{1.7}(PO_4)_3$ ceramics, J. Eur. Ceram. Soc. 36 (2016) 1995–2001, https://doi.org/10.1016/j.jeurceramsoc.2016.02.042.

[25] S. Breuer, D. Prutsch, Q. Ma, V. Epp, F. Preishuber-Pflügl, F. Tietz, M. Wilkening, Separating bulk from grain boundary Li ion conductivity in the sol–gel prepared solid electrolyte $Li_{1.5}Al_{0.5}Ti_{1.5}(PO_4)_3$, J. Mater. Chem. A. 3 (2015) 21343–21350, https://doi.org/10.1039/C5TA06379E.

[26] C.R. Mariappan, M. Gellert, C. Yada, F. Rosciano, B. Roling, Grain boundary resistance of fast lithium ion conductors: comparison between a lithium-ion conductive Li-Al-Ti-P-O-type glass ceramic and a $Li_{1.5}Al_{0.5}Ge_{1.5}P_3O_{12}$ ceramic, Electrochem. Commun. 14 (2012) 25–28, https://doi.org/10.1016/j.elecom.2011.10.022.

[27] S. Soman, Y. Iwai, J. Kawamura, A. Kulkarni, Crystalline phase content and ionic conductivity correlation in LATP glass-ceramic, J. Solid State Electrochem. 16 (2012) 1761–1766, https://doi.org/10.1007/s10008-011-1592-4.

[28] J. Fu, Effects of M^{3+} ions on the conductivity of glasses and glass-ceramics in the system Li_2O-M_2O_3-GeO_2-P_2O_5 (M=Al, Ga, Y, Dy, Gd and La), J. Am. Ceram. Soc. 83 (2000) 1004–1006.

[29] K. Waetzig, A. Rost, C. Heubner, M. Coeler, K. Nikolowski, M. Wolter, J. Schilm, Synthesis and sintering of $Li_{1.3}Al_{0.3}Ti_{1.7}(PO_4)_3$ (LATP) electrolyte for ceramics with improved Li^+ conductivity, J. Alloys Compd. 818 (2020) 153237, https://doi.org/10.1016/j.jallcom.2019.153237.

[30] M. Liu, X. Li, X. Wang, R. Yu, M. Chen, Q. Lu, B. Lu, H. Shu, X. Yang, Facile synthesis and electrochemical properties of high lithium ionic conductivity $Li_{1.7}Al_{0.3}Ti_{1.7}Si_{0.4}P_{2.6}O_{12}$ ceramic solid electrolyte, J. Alloys Compd. 756 (2018) 103–110, https://doi.org/10.1016/j.jallcom.2018.04.333.

[31] N. Kyono, F. Bai, H. Nemori, H. Minami, D. Mori, Y. Takeda, Lithium-ion conducting solid electrolytes of $Li_{1.4}Al_{0.4}Ge_{0.2}Ti_{1.4}(PO_4)_3$ and MO_x (M = Al, Ti, and Zr) composites, Solid State Ionics 324 (2018) 114–127, https://doi.org/10.1016/j.ssi.2018.06.016.

[32] T. Hupfer, E.C. Bucharsky, K.G. Schell, M.J. Hoffmann, Influence of the secondary phase $LiTiOPO_4$ on the properties of $Li_{1+x}Al_xTi_{2-x}(PO_4)_3$ (x=0; 0.3), Solid State Ionics 302 (2017) 49–53, https://doi.org/10.1016/j.ssi.2016.10.008.

[33] E.A. Il'ina, A.A. Raskovalov, N.S. Saetova, B.D. Antonov, O.G. Reznitskikh, Composite electrolytes $Li_7La_3Zr_2O_{12}$-glassy Li_2O-B_2O_3-SiO_2, Solid State Ionics 296 (2016) 26–30, https://doi.org/10.1016/j.ssi.2016.09.003.

[34] E.A. Il'ina, A.A. Raskovalov, B.D. Antonov, A.A. Pankratov, O.G. Reznitskikh, Composite electrolytes ceramic $Li_7La_3Zr_2O_{12}$/glassy Li_2O-Y_2O_3-SiO_2, Mater. Res. Bull. 93 (2017) 157–161, https://doi.org/10.1016/j.materresbull.2017.04.050.

[35] K. Kwatek, W. Ślubowska, J. Trébosc, O. Lafon, J.L. Nowiński, Impact of $Li_{2.9}B_{0.9}S_{0.1}O_{3.1}$ glass additive on the structure and electrical properties of the LATP-based ceramics, J. Alloys Compd. 820 (2020) 153072, https://doi.org/10.1016/j.jallcom.2019.153072.

[36] H. Aono, E. Sugimoto, Y. Sadaoka, N. Imanaka, G. ya Adachi, Electrical property and sinterability of $LiTi_2(PO_4)_3$ mixed with lithium salt (Li_3PO_4 or Li_3BO_3), Solid State Ionics 47 (1991) 257–264, https://doi.org/10.1016/0167-2738(91)90247-9.

[37] K. Kwatek, M. Świniarski, J.L. Nowiński, The Li^+ conducting composite based on $LiTi_2(PO_4)_3$ and Li_3BO_3 glass, J. Solid State Chem. 265 (2018) 381–386, https://doi.org/10.1016/j.jssc.2018.06.028.

[38] K. Kwatek, J.L. Nowiński, Solid lithium ion conducting composites based on $LiTi_2(PO_4)_3$ and $Li_{2.9}B_{0.9}S_{0.1}O_{3.1}$ glass, Solid State Ionics 322 (2018) 93–99, https://doi.org/10.1016/j.ssi.2018.05.007.

[39] K. Kwatek, J.L. Nowiński, Studies on electrical properties of composites based on lithium titanium phosphate with lithium iodide, Solid State Ionics 302 (2017) 35–39, https://doi.org/10.1016/j.ssi.2016.12.007.

[40] N. Sharma, A. Dalvi, Dispersion of Li_2SO_4-$LiPO_3$ glass in $LiTi_2(PO_4)_3$ matrix : assessment of enhanced electrical transport, J. Alloys Compd. 782 (2019) 288–298, https://doi.org/10.1016/j.jallcom.2018.12.153.

[41] N. Sharma, A. Dalvi, Insertion of binary LiCl-P_2O_5 glass between Li^+ NASICON crystallites and its effect on controlling inter-grain transport, Solid State Ionics 342 (2019) 115082, https://doi.org/10.1016/j.ssi.2019.115082.

[42] N.C. Rosero-Navarro, T. Yamashita, A. Miura, M. Higuchi, K. Tadanaga, Preparation of $Li_7La_3(Zr_{2-x},Nb_x)O_{12}$ (x = 0–1.5) and Li_3BO_3/$LiBO_2$ composites at low temperatures using a sol–gel process, Solid State Ionics 285 (2016) 6–12, https://doi.org/10.1016/j.ssi.2015.06.015.

[43] N.C. Rosero-Navarro, A. Miura, M. Higuchi, K. Tadanaga, Optimization of Al_2O_3 and Li_3BO_3 content as sintering additives of $Li_{7-x}La_{2.95}Ca_{0.05}ZrTaO_{12}$ at low temperature, J. Electron. Mater. 46 (2017) 497–501, https://doi.org/10.1007/s11664-016-4924-4.

[44] D. Massiot, F. Fayon, M. Capron, I. King, S. Le Calve, B. Alonso, J. Durand, B. Bujoli, Z. Gan, G. Hoatson, Modelling one- and two-dimensional solid-state NMR, Magn. Reson. Chem. 40 (2002) 70–76, https://doi.org/10.1002/mrc.984.

[45] R. Kahlaoui, K. Arbi, I. Sobrados, R. Jimenez, J. Sanz, R. Ternane, Cation miscibility and lithium mobility in NASICON $Li_{1+x}Ti_{2-x}Sc_x(PO_4)_3$ ($0 < x < 0.5$) series: a combined NMR and impedance study, Inorg. Chem. 56 (2017) 1216–1224, https://doi.org/10.1021/acs.inorgchem.6b02274.

[46] K. Arbi, W. Bucheli, R. Jiménez, J. Sanz, High lithium ion conducting solid electrolytes based on NASICON $Li_{1+x}Al_xM_{2-x}(PO_4)_3$ materials (M = Ti, Ge and $0 < x < 0.5$), J. Eur. Ceram. Soc. 35 (2015) 1477–1484, https://doi.org/10.1016/j.jeurceramsoc.2014.11.023.

[47] H. Yamada, D. Tsunoe, S. Shiraishi, G. Isomichi, Reduced grain boundary resistance by surface modification, J. Phys. Chem. C 119 (2015) 5412–5419, https://doi.org/10.1021/jp510077z.

[48] R. Jimenez, I. Sobrados, S. Martinez-Chaparro, A. Adolfo del Campo, M.L. Calzada, J. Sanz, S.Y. Tsai, M.R. Lin, K.Z. Fung, E. Kazakevičius, A. Kezionis, Preparation and characterization of large area Li-NASICON electrolyte thick films, INORGA 7 (2019) 107–124, https://doi.org/10.3390/inorganics7090107.

[49] B. Raguž, K. Wittich, R. Glaum, Two new, metastable polymorphs of lithium pyrophosphate $Li_4P_2O_7$, Eur. J. Inorg. Chem. 2019 (2019) 1688–1696, https://doi.org/10.1002/ejic.201801100.

[50] R. Bouchet, P. Knauth, J.-M. Laugier, Theoretical analysis of IS of polycrystalline materials with blocking or conducting grain boundaries: from microcrystals to nanocrystals, J. Electrochem. Soc. 150 (2003) E348–E354, https://doi.org/10.1149/1.1580151.

[51] R. Bouchet, P. Knauth, J.M. Laugier, Theoretical analysis of the impedance spectra of electroceramics Part 2: isotropic grain boundaries, J. Electroceram. 16 (2006) 229–238, https://doi.org/10.1007/s10832-006-8278-9.

[52] N.J. Kidner, Z.J. Homrighaus, B.J. Ingram, T.O. Mason, E.J. Garboczi, Impedance/dielectric spectroscopy of electroceramics - Part 2: grain shape effects and local properties of polycrystalline ceramics, J. Electroceram. 14 (2005)

293–301, https://doi.org/10.1007/s10832-005-0968-1.
[53] N.J. Kidner, N.H. Perry, T.O. Mason, E.J. Garboczi, The brick layer model revisited: introducing the nano-grain composite model, J. Am. Ceram. Soc. 91 (2008) 1733–1746, https://doi.org/10.1111/j.1551-2916.2008.02445.x.
[54] N.J. Kidner, Z.J. Homrighaus, B.J. Ingram, T.O. Mason, E.J. Garboczi, Impedance/dielectric spectroscopy of electroceramics-part 1: evaluation of composite models for polycrystalline ceramics, J. Electroceram. 14 (2005) 283–291, https://doi.org/10.1007/s10832-005-0969-0.